ISSN: 2639-7455

Research Article

Earth & Environmental Science Research & Reviews

New solutions for atmospheric and oceanic circulations under Sun-Moon gravitation

Zhiren Wang

Institute of Marine and Coastal Sciences, Rutgers, The State University of New Jersey

*Corresponding author
Zhiren Wang, Institute of Marine and Coastal Sciences, Rutgers, The State University of New Jersey, 71 Dudley Road, New Brunswick, NJ 08901; Email:joewwh77@gmail.com

Submitted: 10 Jan 2019; **Accepted**: 17 Jan 2019; **Published**: 21 Feb 2019

Abstract

By introducing the Sun-Moon gravitation (SMG) into the motions of the atmosphere and oceans and using new methods, I found the gravitation-driven motion (GDM), new solutions, and determined that they contributed to the observed atmospheric-oceanic circulations in structure and variations.

Introduction

The SMG not only controls the orbit of Earth, but also maintain abundant climate variations and structural circulations [1, 2]. General atmospheric circulations such as the Hadley and Walker circulations have been related to inter-annual signals in global climate, with the zonal structure of the circulations being ascribed to the distribution of pressure-zones [3, 8]. Equatorial oceanic currents are believed to be driven by winds and the balance of zonal pressure gradient force and flow acceleration. However, the contribution to circulations from the GDM has been largely omitted. The pressure-zones change in response of the thermal processes and circulations; winds produced smaller equatorial currents than observations; the balance of zonal pressure gradient force and flow acceleration may induce larger equatorial counter currents than observations [this study].

Induced from momentum accumulation on climate scales during the nonlinear interaction between the SMG and moving fluids, the GDM is different from real flows if it is not being balanced out by the omitted factors, and is different than classic tides that have been studied using tidal constituents and harmonic analyses in coastal areas, estuaries, and rivers and solved in a Eulerian system. Tides dissipate the energy in oceans and the solid Earth while slightly reducing the mean motion of the Moon [9, 11]. Tidal-friction interactions and tide-induced residual velocities have been determined to produce new harmonic constituents at frequencies different than those present in disturbing forces, to distort tides in shallow water regions and channels, and to have nonlinear dynamic effects on shallow estuaries, bays, and global oceans [12, 16].

As shown in this study, the GDM also displayed structural circulations, solved in a Lagrangian system for reasons explained in the following section.

Methods

For the climate system, the small SMG accumulatively and actively acts on climate systems over a large space and a long duration. Obtaining an accurate nonlinear solution for the CGIMF within a Eulerian system is difficult because the SMG changes with the relative location between a moving fluid and the Sun or Moon nonlinearly. Pinpointing accurate relative locations, the fast rotation of Earth makes the time step much shorter than that used by classic climate models.

For a numerical model to determine the location, grid spacing in the Eulerian system must be smaller than the distance the float moves within one time step. The longer the temporal scale required to be studied or predicted, the smaller the speed dynamically contributes to a variation on the corresponding temporal scale and a higher resolution is required [1]. If, for example, the time step is one minute and the smallest speed that must be simulated is 0.05m/s (typically for variations of ~10 years, grid spacing must be smaller than 3m [1]. Increasing the time step may enlarge the grid spacing, but results in errors for relative locations and the momentum accumulation effect will be missed.

Resolving the nonlinear SMG effect on climate is still too difficult using a Eulerian system. Longer-term climatic numerical modeling tends to have a lower spatial resolution and a longer time step. On the other hand, due to Earth's fast rotation, a much higher spatial resolution and a much shorter time step are required in order to have the accurate momentum accumulation from slower motions that contribute to longer-term climate variations. The nonlinear system was linearized during the widely applied numerical treatments by setting grid spacing as the distance the fluid moves within one time step, although the grid spacing is usually much larger than the distance when setting flow speed as a constant within each time step and grid spacing and when using smoothing, filtering, and parameterized mixings[1].

To avoid the deformation to the original Newton dynamics during the discretization, here the dynamic equations were established in a Lagrangian system via local coordinates on a rotating Earth, the widely used geostrophic balance approximation was applied, and the widely used linear theory in a Eulerian system was employed to analytically examine the SMG-induced equatorial current system [17,18]. Dissipation took the form of "Rayleigh friction" that fits slow-speed geophysical fluids. After a simplification as performed in Wang et al., the locations of fluids, the Sun, and the Moon were

expressed with the local motion speeds of fluids, the rotation speed of Earth, the orbital obliquities of the Sun and Moon, the Earth's revolution speed, time, and the initial latitudes and longitudes of fluids and the Sun and Moon in local coordinates [1]. The applied dynamic equations are

$$\frac{du}{dt} = v1 f_e \sin\phi - \frac{1}{\rho}\frac{\partial p}{\partial x} - k_f u - \sum_{i=m}^{s} \frac{g_{io}}{4} \sum_{j=1}^{6} (A_j) \sin [q_{uj} t + (X_j)] \quad (1)$$

$$\frac{dv}{dt} = -u1 f_e \sin\phi - \frac{1}{\rho}\frac{\partial p}{\partial y} - k_f v + \sum_{i=m}^{s} \frac{g_{io}}{4} [B_v(t) + \sum_{j=1}^{6} (B_j) \sin [q_{vj} t + (Y_j)] \quad (2)$$

where i = *s*/*m* for the Sun/Moon; *u* and *v* are the zonal and meridional CGIMF components, respectively (u1 and v1 are the real zonal and meridional speed components that maintain geotropic balance), A=[*1,1,k*$_i$, -*k*$_i$,*k*$_i$,-*k*$_i$], B = [-*0.5,0.5,k*$_i$,-*k*$_i$,*k*$_i$,*k*$_i$], B_v = [k_i^2-$k_i^2 cos(2f_{ir}t)$-1] sin [$2R_e^{-1} \int_0^t v\,(t)\,dt + 2\phi$], X =[2λ+ϕ, 2λ-ϕ, λ+ϕ-2f_{ir} t_i , λ-ϕ-2f_{ir} t_i λ-ϕ, λ+ϕ], Y=[2λ+ 2ϕ, 2λ-2ϕ, λ+2ϕ-$f_{ir\ ti,}$ λ-2ϕ-2$f_{ir\ ti,}$ λ+2ϕ]. Other parameters were described in Wang et al. [2012A].

Structural GDM for atmospheric and oceanic circulations

Structural GDM for atmospheric circulations

Figure 1 depicts the GDM for the atmosphere modeled from Eq. 1 and 2 that were integrated for 10 years with a 60s time step, for different initial speeds, using a dissipation coefficient of 3×10^{-8} s^{-1} (similar structures were obtained using 6 to 600s time steps and 3×10^{-9} to 120×10^{-9} s^{-1} dissipation coefficients). The GDM will reach a speed of 20ms^{-1} after accumulating for four to seven years around ±35° and ±65°, for nine to ten years at other latitudes, and for only two years near 30 ±5° with an extremely strong initial eastward flow of 20m/s, showing the observed asymmetry for zonal flow.

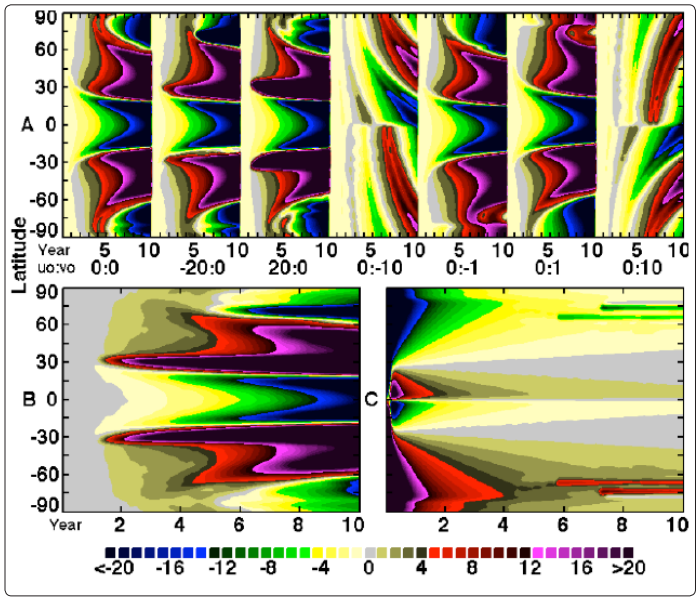

Figure 1: Structural atmospheric GDM against time (year, the first x-axis) and latitude (y-axis) at different initial speeds (uo:vo, m/s, the second x-axis in **A**), computed from the Eq. 1 and 2 for u (m/s, **A** and **B**) and v (cm/s, **C**) GDM components. **B** and **C** were averaged for all the initial speeds as listed in **A**.

The general structures for long-term GDM can be summarized as follows:

1. Some of the SMG component pointed toward the point-blank latitude, producing equator-ward and westward motion at lower latitudes under geostrophic conditions.
2. The zonal GDM structures were consistent with observations. The mean zonal GDM was easterly in low latitudes from approximately 19±2°S to 19±2°N, westerly in the mid-latitudes from approximately 19±2°S/N to 63±12°S/N, and easterly in high-latitudes higher than approximately 63±12°S/N. The mean observed zonal atmospheric circulations displayed a similar structure (Figure 3).
3. The zonal structure of the GDM was eventually maintained and could be established either from a static or moving atmosphere. The zonal speed was much smaller than Earth's rotational speed (i.e., |u|<<460 *cos* ϕ), and, therefore, had little affect on the structure of the GDM, except near the poles where the structure of the GDM varied with the initial zonal speed and temporal scales. At high latitudes, the observed weather-climate systems also varied considerably.
4. A usual initial northward (southward) meridional wind (e.g., ± 1 m/s) moved the zonal belt of the GDM northward (southward) (e.g., by ~3°), likely being related to the latitudinal shift of the intertropical convergence zone. An irregularly strong initial meridional speed could temporarily mix up the zonal belt structure of the GDM, which was consistent with observations: the adjustment from a normal phase to an unstable El Niño phase accompanies with an intensified Hadley circulation or an abnormally enhanced meridional speed component [Wang et al., 2012B].

Structural GDM for oceanic currents

Figure 2 depicts the GDM for oceans modeled from Eq. 1 and 2 that were integrated for 10 years at different initial speeds, using a dissipation coefficient of 10^{-6} s^{-1} (similar structures were obtained using values of 10^{-8} to 10^{-6} s^{-1}). There are northern and southern horizontal boundaries set at latitudes of 60°S and 60°N.

After accumulating for approximately four years, the GDM will reach a speed of approximately 3m/s. A stable latitudinal structure of the zonal GDM was maintained, hardly dependent of initial currents. The mean zonal GDM was eastward in equatorial zones from approximately 10°S to 10°N, was westward in latitudes from approximately 10°S/N to 30°S/N, and was eastward in latitudes 30°S/N to 60°S/N. This current structure is approximately similar with the observations for the Pacific and Atlantic Oceans (Figure 3).

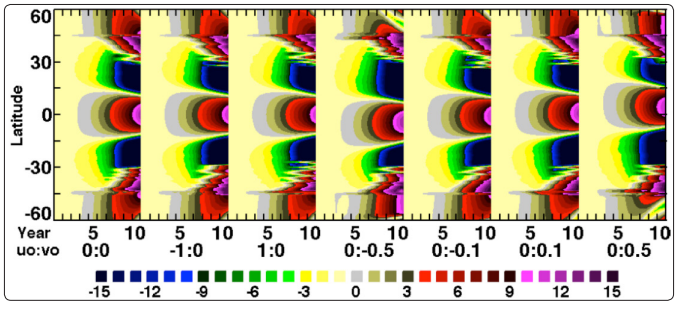

Figure 2: Structural oceanic zonal GDM (m/s) against time (year, the first x-axis) and latitude (y-axis) at different initial speeds (uo : vo, m/s, the second x-axis), computed from the Eq. 1 and 2.

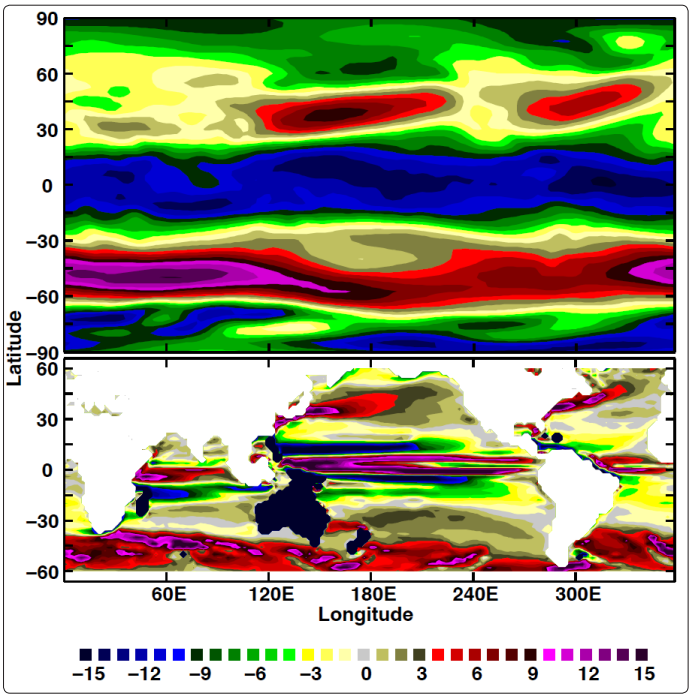

Figure 3: Observed atmospheric (above) and oceanic circulations (below): Atmospheric zonal mass flux (wind times density, $kgs^{-1}m^{-2}$) was averaged from 1980-2009 and within 100-1,000hPa. Oceanic current (cm/s) was averaged from 1980-2009 and within 5-225m. Data were obtained from the Physical Sciences Division, Earth System Research Laboratory, NOAA (www.esrl.noaa.gov/psd).

The mean zonal current is eastward in equatorial zones from approximately 4°S to 10°N with the zones extending to 10°S near western and eastern Pacific Ocean, is westward in latitudes from approximately 10°N to 30°N and from approximately 4−10°S to 21−39°S, and is eastward in latitudes from approximately 30°N to 53−60°N and from approximately 21−39°S to 60°S. For the Indian Ocean with narrower northern and southern horizontal boundaries at approximately 60°S and 22°N, however, there was a larger difference in zonal currents between the GDM and observation although the similar latitudinal structure was still kept in both the GDM and observation. Omitted topography (e.g., west-east boundaries) and thermohaline may have lost the observed details in the GDM. The similar structures between the GDM and observed currents suggest that the GDM may contribute to oceanic currents, including the equatorial current system, which was supported by the following examinations.

Equatorial currents reexamined using data and a linear theory

Equatorial currents compose of the south/north equatorial currents (SEC/NEC) and the equatorial counter currents (ECC) (e.g., [Knauss, 2005]). Using Ekman theory, the wind-induced water-transport flux within a latitudinal cross section from y1 to y2 is summarized, as follows:

$$F_{lux} = \int_{y1}^{y2} \frac{\rho_a C_D U_a v_a}{\rho f} dy \qquad (3)$$

where U_a and v_a are sea-surface wind speed and its meridional component, respectively, $f = 1.458\times10^{-4}\times\sin(y/R_e)$ s^{-1} (Coriolis parameter), ρ_a=1.29 kg/m^3 (sea-surface air density), ρ=1025 kg/m^3 (water density), and C_D=0.0015 (maximum sea-surface drag coefficient).

Averaged from 1993-2009, the SEC/NEC from winds within the Pacific Ocean was estimated to be -0.7/-0.6Sv (1Sv=10^6 m^3/s), contributing only 5.6/3.7 % to the observed SEC/NEC (the largest contribution estimated from maximum wind was no more than 52/18%, Figure 4A and B). The wind stress used for estimating the SEC/NEC was approximately -33%/69% correlated to the observed SEC/NEC (at a 95% confidence level, using t-test), which implies that winds can't fully explain the observed SEC/NEC.

The balance between current acceleration and zonal gradient force (ZGF=-g∂h/∂x) within equatorial zone where the Coriolis force is close to zero is as

$$\partial ECC / \partial t = -g\partial h / \partial x \qquad (4)$$

where h is the sea-level height, and g = 9.8ms^{-2}.

The ZGF averaged within equatorial zone was below zero during El Niño phase in (1992)/1993, 1994/1995, 1997/1998, 2002/2003, 2006/2007, and 2009/2010, but was above zero during non El Niño (normal and La Niña) phases, showing the coherence to an ENSO cycle (Figure 4C).

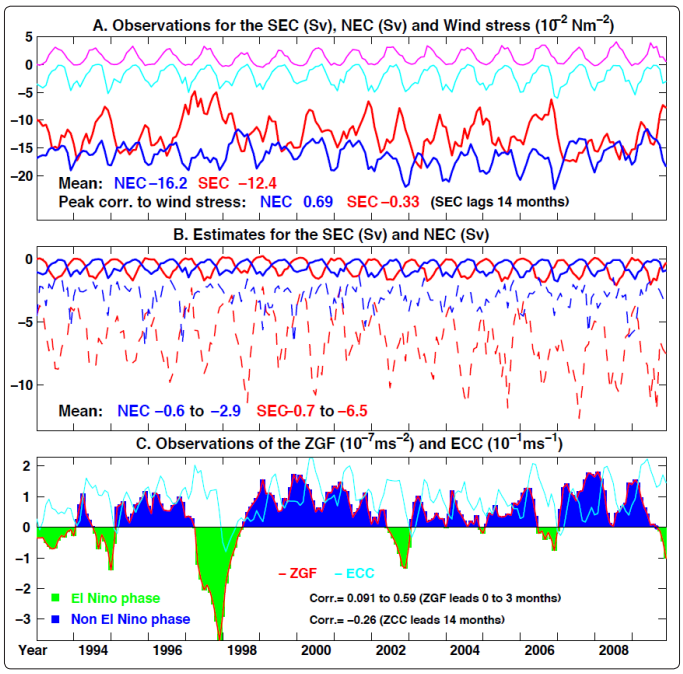

Figure 4: (A) Observations for monthly fluxes of the south/north equatorial currents (SEC/NEC) computed from the observed oceanic currents averaged within 120-280°E, 2.5-10°S/10-20°N, and 0−225m depth (magenta/cyan curve is the wind stress for the estimated SEC/NEC), **(B)** estimates for the SEC/NEC computed using Eq. 3 from sea-surface winds (dashed lines were the maximum estimates using the maximum winds) within 120-280°E and 2.5-10°S/10-20°N), and **(C)** observations for the zonal gradient force (ZGF) and equatorial counter current (ECC) computed from the observed sea-level height and oceanic currents averaged within 148-272°E, 4°S−10°N, and 0−225m depth. The sea-level height was obtained from the altimeter products of Aviso (www.aviso.oceanobs.com)

and the oceanic currents and winds were obtained from the same source as Figure 3.

If the ECC were only from the balance of current acceleration and the ZGF, the ZGF should immediately project and highly correlate to the ECC (it takes only a few weeks for the ECC to be integrated to 0.1 m/s, with ZGF≈ 10^{-7}m/s^2 using Eq. 6). However, there was no instantaneous correlation (correlation coefficient was 0.091) between the ZGF and ECC unless the ZGF leads the ECC by three months with a correlation coefficient 0.59, implying that the ZGF must be established prior to the ECC. The ECC may change the ZGF through transporting water, and negatively correlate to the ZGF. However, a low peak correlation -0.26 existed with ZCC leading approximately 14 months. During, e.g., 1999−2001, the mean ZGF was continuously positive with a mean value of 1.02×10^{-7} m/s^2, which would produce an abnormally large ECC (approximately 9.7m/s) if ECC were produced only from the balance between current acceleration and the ZGF.

Therefore, the NEC and SEC produced by winds were much weaker than their observations, and the observed ECC may not be induced only from the balance between current acceleration and the gradient force. The GDM was lasting and independent of winds, and may be one of the drivers for equatorial currents with the general zonal GDM consistent with the observed equatorial current systems in latitudinal structure. The variations of the NEC and SEC (off-equator) and ECC (near-equator) and their fluxes will be computed using barotropic oceans under the SMG and the angular momentum conservation. After introducing the SMG into the linearized and daily averaged shallow water equations, the basic controlling equation is

$$\frac{f_e}{2\pi}(v[D_2]-v[D_1]) - \frac{g}{R_e}\frac{\partial H}{\partial \phi} - fu =$$

$$\frac{\sin 2\phi}{4}\sum_{i-M}^{S} g_{io}[1-k_i^2 - \frac{f_{ir}\cos(t_c-2\lambda)}{f_e-f_{ir}} + \frac{4k_i f_{ir}\, ctg2\phi}{f_e-2f_{ir}}\sin(t_c-\lambda) + k_i^2\cos t_c] \quad (5)$$

where u, v, and H are daily mean zonal speed, meridional speed, and water thickness, respectively, $D_1 = 2\pi\, n_t / f_e$, $D_2 = 2\pi\, t\,(n_t+1)/f_e$, other parameters were described in [Wang et al., 2012A].

The equatorial zone with latitude $\phi \in [-\phi_h, \phi_h]$ (here, ϕ_h =20°) is divided into near-equator zone with latitude $\phi \in [-\phi_e, \phi_e]$ (here ϕ_e=7°) and off-equator zone with latitude $\phi \in [\phi_e, \phi_h]$ $[-\phi_h, -\phi_e]$ (∪ represents logic "and"). The off-equator currents are derived directly from Eq. 5

$$u = -cos\phi \sum_{i-M}^{S} \frac{g_{io}}{4f_e}[1-k_i^2(1-cos_{tc}) - \frac{f_{ir}cos(t_c-2\lambda)}{f_e-f_{ir}} + \frac{4k_i f_{ir} ctg2\phi}{f_e-2f_{ir}} sin(t_c-\lambda)]$$

$$+\frac{g}{2f_e R_e sin\phi}\frac{\partial H}{\partial \phi} + \frac{1}{4\pi sin\phi}(v[D_2]-v[D_1]) \quad (6)$$

Within the off-equator zone where Coriolis force is not zero, the equator-ward SMG produced westward currents, linearly estimated as -1 to -2/-2 to -4 mm/s under the gravitation of the Sun/Moon, as depicted in Figure 5a/c. The mean flux under the SMG was approximately -20.8Sv across a section of 0−2000m depth, 10o −20°S, and 10°N−20°N comparable to the mean observed SEC plus NEC that is approximately -28.7Sv, with a correlation of 0.48 (at confidence 95% level using t-test) (Figure 5e). The angular momentum of the entire air and sea relative to the rotating Earth can be conserved on the short range of climatic temporal scale. With $R_e >> H$, the angular momentum conservation equation can be written, as follows:

$$\int_0^{\phi_e}\left[f_n(\lambda,\phi,t)+f_n(\lambda,-\phi,t)\right]d\phi + \int_{\phi_e}^{\phi_h}$$

$$\left[f_n(\lambda,\phi,t)+f_n(\lambda,-\phi,t)\right]d\phi + A_n = C_o \quad (7)$$

where, $f_n(\lambda,\phi,t) = \rho\, cos^2\phi u(\lambda,\phi,t)H(\lambda,\phi,t)$, C_o is a constant, A_n is the total relative angular momentum input into the oceans within zone $\phi\in[-\phi_h, \phi_h]$ from the atmosphere and the solid Earth. Substitute u in Eq. 6 to the u in Eq. 7 for zones $\phi \in [\phi_e\ \phi_h] \cup [-\phi_h - \phi_e]$, the averaged near-equator zonal current is estimated as

$$u_e \equiv \frac{1}{2\phi_e}\int_{-\phi_e}^{\phi_e} u(\phi)d\phi$$

$$= A_m \sum_{i-M}^{S}\frac{g_{io}}{f_e}[\,1 - k_i^2(1-cos_{tc}) - \frac{f_{ir}cos(t_c-2\lambda)}{f_e-f_{ir}} + \frac{k_i\, f_{ir}Csin(t_c-\lambda)}{f_e-2f_{ir}}] \quad (8)$$

where, $A_M = R_h[9sin\,\phi_h + \sin(3\,\phi_h) - 9\sin\,\phi_e - \sin(3\phi_e)]\ /\ [24\,\phi_e + 12sin(2\,\phi_e)]$ (amplification coefficient for the SMG-induced near-equator zonal current), $R_h \equiv H_h\,\rho_h / (H_e\,\rho_e)$ (the ratio of mass in unit horizontal area of off-equator to near-equator seawater), *He* and ρ_e are water depth and density averaged within $[-\phi_e, \phi_e]$, respectively, H_h and ρ_h are water depth and density averaged within $[\phi_e, \phi_h] \cup [-\phi_h, -\phi_e]$, respectively, $C=24\ [Q+2(cos\phi_h^{\,3} - cos\phi_e^{\,3}/3]\ [9(sin\phi_h - sin\phi_e) + sin3\phi_h) - sin3\phi_e)]$, and $Q = cos\phi_h - cos\phi_e + log(ctg\frac{\phi_e}{2}tg\frac{\phi_h}{2})$.

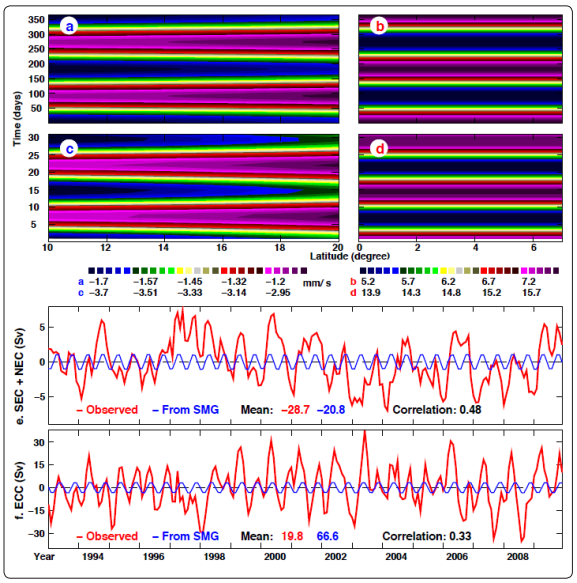

Figure 5: Equatorial zonal current (mm/s) induced by the gravitations of the Sun (**a−b**) and Moon (**c−d**) against latitudes (degree, x-axis for both hemispheres) and time (day, y-axis), as described in Eq. 6 and 8. (**e**) The observed/SMG-induced anomalies (red/blue curve, in Sv) of the north equatorial current (NEC) plus the south equatorial current (SEC) across a section of 0−2000m depth, 10°S −20°S and 10°N−20°N. (f) The equatorial counter current (ECC) across

a section of 0−2000m depth and 7°S−7°N. The observed oceanic currents were obtained from the same data source as Figure 3.

The g_{io} item in Eq. 8 is the SMG-induced eastward near-equator current. For oceans with even depth and density, R_h =1. According to TOPEX monthly mean sea level data, $R_h \approx 0.91$ and $A_m \approx$ **0. 63** for Indian Ocean where the ECC was weakened with a narrow basin, $R_h \approx 1.0$ and $A_m \approx$ **1. 1** for Pacific and Atlantic oceans where the ECC was amplified with a wide basin. Linearly estimated, the SMG-induced ECC was approximately 5−8/14−**16** mm/s under the gravitation of the Sun/Moon (Figure 5 b/d) if near-equator current was limited within a zone from 7°S to 7°N (the narrower this zone, the stronger the SMG-induced ECC was, under the angular momentum conservation). Mean flux from the SMG-induced ECC was approximately 66Sv within a section of 0−2000m depth and 7°S−7°N, even larger than the flux (~20Sv) from the observed ECC if not balanced with the omitted factors. The correlation between the SMG-induced and observed fluxes was 0.33 (at confidence 95% level using t-test) (Figure 5f).

Discussion

Will a stable ENSO cycle be maintained? Will long-term climate present the permanent El Niño-like pattern as determined in paleoclimate studies [Koutavas et al., 2002; Wara et al., 2005]? The stable and unceasing momentum accumulation through the structural GDM may contribute to maintaining a lasting westward current in the tropics, leading to a longer La Niña-like pattern of ENSO, as far as the dynamics are concerned. For the past half century, the normal-La Niña phase was always longer than the El Niño phase, and the transformation from a La Niña to an El Niño phase was a relatively faster circulation adjustment [Wang et al., 2012B].

However, it is still unknown on what extent and for how long can the slow accumulative GDM adjust a circulation from an abnormal phase (e.g., El Niño with an abnormally enhanced meridional circulation component) to a regular phase (e.g., La Niña with a quasi-zonal circulation) because circulations are also locally and temporarily controlled by weather systems.

The model used for this study emphasized the SMG-dynamics and accumulative effects on climate. The lack of thermodynamics, baroclinic processes, thermohaline, and geotropic departure, however, must have made the SMG-induced currents and fluxes depart from their observations. After all, a small fraction of kinetic energy can transport huge amount of energy (e.g., a latent energy of up to 10,000 times the kinetic energy of wind itself can be transported by the wind, depending on air humidity and wind speed) and a small change in circulations may cause large weather-climate adjustment.

Current climate models can hindcast historical climate well over long periods [Chen et al., 2004] because they are driven by observed variables (e.g., climatological and monthly temperature, winds, and heat fluxes) that already include the temporal frequencies and spatial circulation structures induced from all real processes including the omitted ones. However, missed dynamic information for the prediction windows compromises accurate prediction, with prediction uncertainties arising quickly and increasing with prediction length [Stainforth et al., 2005]. Accumulated momentum from the GDM can "automatically" be included in the observed winds and currents for the hindcasting window, but not for predication windows.

Uncertainties come up so soon within predication windows that dynamics may be of larger "suspicion" than slow processes (e.g., GHGs) and well-done thermodynamics for causing uncertainties. Solving the SMG-Eulerian dilemmas, introducing the SMG-dynamics, using much higher resolution models, and developing new discretization methods would improve climate studies and forecasts. The tasks for studying, understanding and forecasting our climate-environment is pressing and overwhelming.

References

1. Wang Z, D Wu, X Song, X Chen, S Nicholls (2012A) Sun-Moon Gravitation Induced Wave Characteristics and Climate Variation. J. Geophys. Res doi.org/10.1029/2011JD016967.
2. Wang Z, X Lin (2015) Astronomy and Climate-Earth System: Can Magma Motion under Sun-Moon Gravitation Contribute to Paleoclimatic Variations and Earth's Heat? Advances in Astronomy doi: 10.1155/2015/536829.
3. Hadley G (1735) on the cause of the general trade winds, Phil. Trans. Roy. Soc 34: 58-62.
4. Walker G (1923) Correlation in seasonal variation of weather. VIII. A preliminary study of world weather. Memoirs of the Indian Meteorological Department 24: 75-131.
5. Grove R H (1998) Global Impact of the 1789–93 El Niño, Nature 393: 318-319.
6. Moore A M, R Kleeman (1999) Stochastic forcing of ENSO by the intraseasonal oscillation, J. Clim12: 1199-1220.
7. Perigaud C M, C Cassou (2000) Importance of oceanic decadal trends and westerly wind bursts for forecasting El Niño. Geophys. Res. Lett 27: 389-392.
8. Boulanger J P (2001) Role of non-linear oceanic processes in the response to westerly wind events: New implication for the 1997 El Niño. Geophys. Res. Lett 28:1603-1606.
9. Cheng M K, R J Eanes, B D Tapley (1992) Tidal deceleration of the Moon's mean motion. Geophys. J. Int 108: 401-409.
10. R D Ray, R J Eanes, B F Chao (1996) Detection of tidal dissipation in the solid earth by satellite tracking and altimetry. Nature 381: 595-597.
11. Egbert G D, R D Ray (2000) significant dissipation of tidal energy in the deep ocean inferred from satellite altimeter data. Nature 405: 775-778.
12. Proudman J (1923) Tides: Appendix. Reports on the State of Science, Section A-Liverpool, P1-6, British Association.
13. Kabbaj A, C LeProvost (1980) Nonlinear Tidal Waves in Channels: A Perturbation Method Adapted to the Importance of Quadratic Bottom Friction, Tellus 32: 143-163.
14. Gallagher B S, W H Munk (1971) Tides in Shallow Water: Spectroscopy, Tellus 23: 346-363.
15. Hunt J N, B Jonhns (1963) Currents induced by tides and waves, Tellus 15: 343-351.
16. Kantha L H (1995) Barotropic tides in the global oceans from a nonlinear tidal model assimilating altimetric tides. J. Geophys. Res 101: 25283-25308.
17. Knauss J A (2005) An Introduction to Physical Oceanography, 2nd Ed., Waveland Press Inc 309p.
18. Wallace J, P V Hobbs (2006) Atmospheric Science - An Introductory Survey. 2nd Ed. Academic Press 483p.
19. Wang Z, D Wu, X Chen, R Qiao (2012B) ENSO Indices and Analysis, Adv. in Atmosph. Sci 30: 1491-1506.
20. Koutavas A, L S Jean, T M Marchitto, J P Sachs (2002) El Niño–Like Pattern in Ice Age Tropical Pacific Sea Surface Temperature. Science 297: 226-229.

21. Wara MW, Ravelo AC, Delaney ML (2005) Permanent El Niño–Like Conditions During the Pliocene Warm Period. Science 309: 758-761.
22. Chen D, Cane MA, Kaplan A, Zebiak SE, Huang D (2004) Predictability of El Niño over the past 148 years, Nature 428:733-736.
23. D A Stainforth, T Aina, C Christensen, M Collins, N Faull (2005) Uncertainty in predictions of the climate response to rising levels of greenhouse gases. Nature 433: 403 406.